Se-NiSe$_2$ hybrid nanosheet arrays with self-regulated elemental Se for efficient alkaline water splitting

Xiang Peng [a,b], Yujiao Yan [a], Shijian Xiong [a], Yaping Miao [c], Jing Wen [a], Zhitian Liu [a,*], Biao Gao [b,d,**], Liangsheng Hu [e], Paul K. Chu [b,*]

[a] Hubei Key Laboratory of Plasma Chemistry and Advanced Materials, Hubei Engineering Technology Research Center of Optoelectronic and New Energy Materials, Wuhan Institute of Technology, Wuhan 430205, China
[b] Department of Physics, Department of Materials Science and Engineering, Department of Biomedical Engineering, City University of Hong Kong, Tat Chee Avenue, Kowloon, Hong Kong, China
[c] School of Textile Science and Engineering, Xi'an Polytechnic University, Xi'an 710048, China
[d] State Key Laboratory of Refractories and Metallurgy, Institute of Advanced Materials and Nanotechnology, Wuhan University of Science and Technology, Wuhan 430081, China
[e] Department of Chemistry, Key Laboratory for Preparation and Application of Ordered Structural Materials of Guangdong Province, Shantou University, Shantou 515063, China

ARTICLE INFO

ABSTRACT

Understanding the catalytic mechanism of non-noble transition metal electrocatalysts is crucial to designing high-efficiency, low-cost, and durable alternative electrocatalysts for water splitting which comprises the hydrogen evolution reaction (HER) and oxygen evolution reaction (OER). In this work, Se-NiSe$_2$ hybrid nanosheets with a self-regulated ratio of ionic Se (I-Se) to elemental Se (E-Se) are designed on carbon cloth by solution synthesis and hydrothermal processing. The effects of the I-Se/E-Se ratios on the electrocatalytic characteristics in HER and OER are investigated systematically both experimentally and theoretically. The optimized bifunctional electrocatalyst needs overpotentials of only 133 mV to deliver an HER current density of 10 mA cm^{-2} and 350 mV to generate an OER current density of 100 mA cm^{-2} in 1.0 mol L^{-1} KOH. Based on the density-functional theory calculation, surface-adsorbed E-Se is beneficial to optimizing the electron environment and the adsorption/desorption free energy of hydrogen/water of the hybrid catalyst, consequently facilitating the electrocatalytic water splitting process. There is a proper I-Se/E-Se ratio to improve the catalytic activity and kinetics of the reaction and the optimized E-Se adsorption amount can balance the interactions between I-Se and E-Se, so that the catalyst can achieve appropriate Se-H binding and active site exposure for the excellent electrocatalytic activity. To demonstrate the practicality, the assembled symmetrical device can be powered by an AA battery to produce hydrogen and oxygen synchronously. Our results provide a deeper understanding of the catalytic mechanism of transition metal selenides in water splitting and insights into the design of high-efficiency and low-cost electrocatalysts in energy-related applications.

© 2022 Published by Elsevier Ltd on behalf of The editorial office of Journal of Materials Science & Technology.

1. Introduction

Water electrolysis is one of the attractive hydrogen production techniques for green and sustainable energy because of zero carbon emission, high hydrogen purity, and relatively simple operation [1,2]. Electrochemical water splitting encompasses the cathodic hydrogen evolution reaction (HER) and anodic oxygen evolution reaction (OER) [3,4]. In both reactions, electrocatalysts are required to boost the efficiency and a myriad of electrocatalysts that can decrease the energy barrier and expedite the reaction kinetics have been proposed [5–8]. Up to now, Pt-group metals and alloys are effective HER catalysts and compounds comprising Ir and Ru are regarded to be efficient OER catalysts. However, the natural scarcity and high cost of these noble elements impact commercial application [9] and therefore, there is an urgent need to develop alternative electrocatalysts with high efficiency and low cost, es-

* Corresponding authors.
** Corresponding author at: Hubei Key Laboratory of Plasma Chemistry and Advanced Materials, Hubei Engineering Technology Research Center of Optoelectronic and New Energy Materials, Wuhan Institute of Technology, Wuhan 430205, China.
E-mail addresses: able.ztliu@wit.edu.cn (Z. Liu), gaobiao@wust.edu.cn (B. Gao), paul.chu@cityu.edu.hk (P.K. Chu).
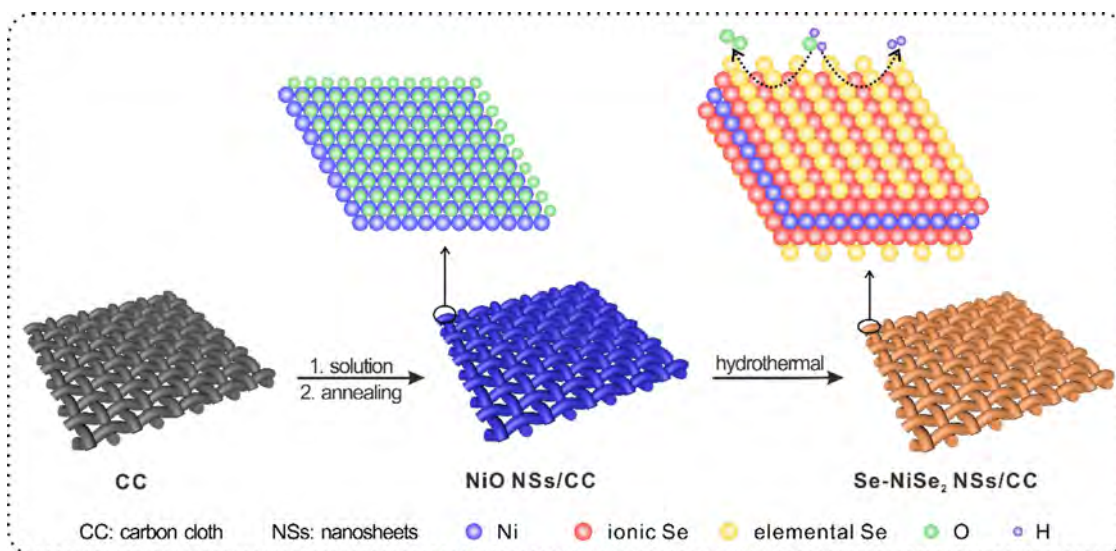
Scheme 1. Schematic illustration of the preparation of the Se-NiSe$_2$ hybrid nanosheet electrocatalyst and application as a bifunctional water splitting electrocatalyst.

pecially compounds composed of non-noble transition metals with tunable d-electron configurations [10–14].

Among the various transition metal compounds, transition metal selenides not only have abundant electronic states, but also show excellent flexibility and regulation in terms of the structure and functions which can be exploited in HER, OER, water oxidation [15], hydrogenation, and detection [16]. For instance, nickel selenide is one of the effective electrocatalysts for water splitting due to its good activity (intrinsic electronic structure), easy fabrication, low cost, metallic nature, and excellent electrical conductivity [17,18]. For instance, Liang et al. have reported that NiSe$_2$ nanoparticles have high HER activity comparable to that of Pt as well as stability [19]. Wang et al. have observed that elemental Se (labeled as E-Se) formed during the synthesis of nickel selenide, and adsorption on the NiSe$_2$ surface leads to efficient conversion of H$^+$ into H$_2$ and facilitates charge transfer during HER [20]. Zhou et al. have also proposed that a small fraction of E-Se on the surface of pyrite NiSe$_2$ can increase the catalytic sites in HER [21]. However, the interactions between ionic Se (labeled as I-Se) and E-Se as well as the mechanism of E-Se are not clear. Since Se sites have been shown to be active catalytically [20], adsorbed E-Se may also play an important role in the electrocatalytic reactions and so it is important to elucidate the roles of I-Se and E-Se on selenides. Unfortunately, up to now, no systematic study has been reported to fabricate Se-NiSe$_2$ hybrids with controllable I-Se/E-Se ratios and investigate the influence of the I-Se/E-Se ratios and associated mechanism in water splitting.

In this work, Se-NiSe$_2$ hybrid nanosheets with self-regulated I-Se/E-Se ratios are produced controllably on carbon cloth (NiSe$_2$/CC) as high-performance bifunctional catalysts for both HER and OER, as schematically illustrated in Scheme 1. The I-Se/E-Se ratios can be tuned by the hydrothermal temperature, and the characteristics and mechanism are evaluated systematically experimentally and theoretically. The optimized bifunctional electrocatalyst needs overpotentials of only 133 mV to deliver an HER current density of 10 mA cm^{-2} and 350 mV to generate an OER current density of 100 mA cm^{-2} in 1.0 mol L^{-1} KOH. Based on the density-functional theory calculation, surface-adsorbed E-Se alters the electron environment and adsorption/desorption free energy of hydrogen/water of the hybrid catalyst, consequently facilitating the electrocatalytic water splitting process. For a demonstration of the practical potential, the symmetrical device constructed with NiSe$_2$/CC as both the anode and cathode can be powered by an AA battery to conduct overall water splitting. The results provide a clearer understanding of the electrocatalytic mechanism of transition metal selenides in overall water splitting.

2. Experimental details

2.1. Materials preparation

The nickel-based precursor nanosheets were grown on carbon cloth (CC) by a solution technique. Typically, 4.2 g of NiSO$_4$·6H$_2$O and 0.81g of K$_2$S$_2$O$_8$ were dissolved in 28 mL of deionized water (DW) and stirred. A piece of clean CC (2 cm × 3 cm) was immersed into the solution and 4 mL of ammonium hydroxide (28%–35%) was dropped and stirred for another 20 min. The CC was washed with DW three times before vacuum drying and the sample was designated as Ni-OH/CC. Ni-OH/CC was calcinated at 300 °C for 30 min in air to stabilize the nanostructure and convert nickel hydroxide into NiO (NiO/CC). To convert the nickel oxide into selenide, NiO/CC was subjected to a hydrothermal reaction in an aqueous solution (2 mL of DW and 36 mL ethanol) containing Se powder and NaBH$_4$ at 140–200 °C for 8 h. After cooling to room temperature, the sample was taken out and washed with DW. The final Se-NiSe$_2$ hybrid nanosheet electrocatalysts were designated as NiSe$_2$/CC-n, where n represents the hydrothermal temperature.

2.2. Materials characterization

The morphology of the samples was examined by scanning electron microscopy (SEM, Hitachi SU 3500) and transmission electron microscopy (TEM, Titan G260-300). The crystal structure and composition were characterized by X-ray diffraction (XRD, LabX XRD-6100, Shimadzu), high-resolution TEM (HR-TEM), Raman scattering (HR RamLab) and X-ray photoelectron spectroscopy (XPS, Thermo Scientific K-Alpha, Thermo Fisher) using monochromatic Al K_α X-ray.

2.3. Electrochemical measurement

The electrochemical measurements were performed on the CHI 660E electrochemical workstation using a standard three-electrode system in 1.0 mol L^{-1} KOH. Linear sweep voltammetry (LSV) was conducted at a scanning rate of 5 mV s^{-1} to investigate the HER, OER, and overall water splitting activity. In the assessment,
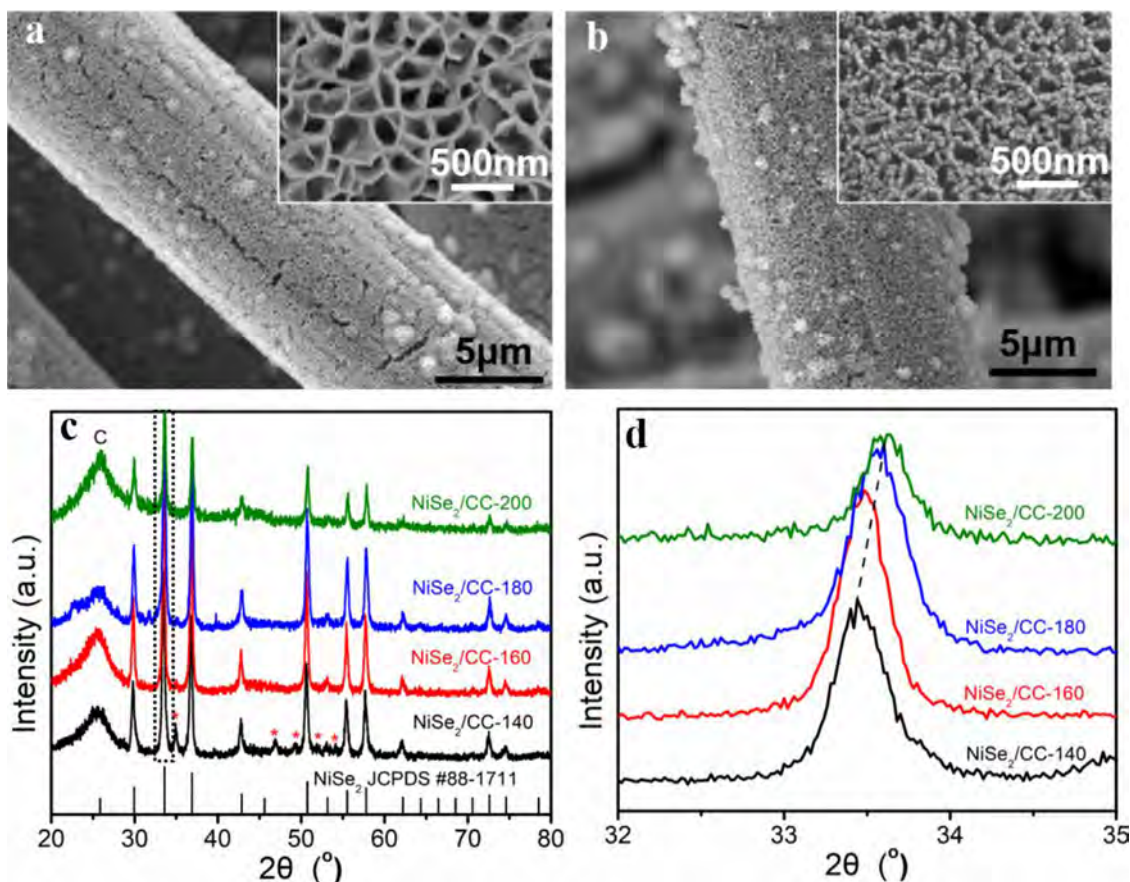
Fig. 1. SEM images: (a) Ni-OH/CC and (b) NiSe$_2$/CC-180 with the insets showing the corresponding high-resolution images; (c) XRD patterns (* representing orthorhombic NiSe$_2$, JCPDS No. 18-0886) and (d) selected patterns from the dotted rectangular box in (c) of NiSe$_2$/CC selenized at different temperatures.

a saturated calomel electrode (SCE) was the reference electrode and all the potentials were *iR* corrected and calibrated to the reversible hydrogen electrode (RHE) according to Nernst equation: $E_{RHE} = E_{SCE} + 0.242 + 0.059pH$, where the pH of 1 mol L^{-1} KOH aqueous solution was measured to be 13.78 with a pH meter (FE28, Mettler Toledo). The Tafel slopes were plotted as overpotentials (η) vs. log currents (log|j|) derived from the polarization curves. The electrochemical active surface areas (ECSA) were determined by cyclic voltammetry (CV) in the voltage range from -0.4 to -0.5 V vs. SCE at various scanning rates (10-100 mV s^{-1}). Electrochemical impedance spectroscopy (EIS) was performed at an initial potential of -1.3 V vs. SCE for HER and 0.6 V vs. SCE for OER, respectively. The stability test was carried out by the chronoamperometric method at a constant voltage.

3. Results and discussion

3.1. Synthesis and characterization of electrocatalysts

Scheme 1 illustrates the preparation of the NiSe$_2$/CC electrocatalysts by the solution method and hydrothermal reaction. After preparing nickel hydroxide on CC, the samples are annealed to stabilize the crystal structure [22]. During the hydrothermal process, NiO is converted into NiSe$_2$ and elemental Se (E-Se) adsorbed onto the surface impacts the catalytic activity [20,21]. The SEM images in Fig. 1(a) show nanosheet arrays on the carbon fiber of CC. After annealing at 300 °C, no obvious morphological change can be found as shown in Fig. S1 in Supplementary Information. The nanosheets roughen after selenization process but the structure of surrounding nanosheets is maintained (Figs. 1(b) and S2).

Nanosheets with a rough and porous surface tend to expose more active sites to enhance the catalytic activity.

The crystal structure and composition of the samples are determined by XRD. The diffraction pattern of the solution product (Fig. S3) matches those of γ-NiOOH (JCPDS card No. 06-0075) and β-Ni(OH)$_2$ (JCPDS card No. 14-0117) consistent with previous literature [23]. After annealing in air at 300 °C, nickel hydroxide is converted into NiO (JCPDS card No. 04-0835) Fig. 1(c) shows the XRD patterns after hydrothermal selenization at different temperatures. At a high temperature, beside the broad peak at 25° originating from CC [10,24], the other diffraction peaks can be attributed to high-purity NiSe$_2$ (cubic, JCPDS card No. 88-1711), indicating complete conversion from NiO to NiSe$_2$. However, at a low temperature, orthorhombic NiSe$_2$ (JCPDS No. 18-0886) is detected similar to the previous results [25]. The diffraction peaks of NiSe$_2$ change after the hydrothermal treatment at different temperatures as shown in Fig. 1(d). For example, they shift to smaller angles at a low hydrothermal temperature thus suggesting some degree of lattice expansion which may facilitate charge transfer and enhance the electrochemical activity.

The TEM image in Fig. 2(a) corroborates the porous nanosheet structure after selenization in line with SEM. The HR-TEM image in Fig. 2(b) indicates a lattice distance of 0.27 nm for NiSe$_2$ (210). Beside the crystalline component, the amorphous component can be detected from NiSe$_2$/CC-180 as shown by the areas enclosed by yellow dots in Fig. 2(b). The elemental maps in Fig. S4 disclose that Ni and Se are distributed uniformly. Nitrogen adsorption-desorption was carried out to determine the specific surface area and pore size distribution of the NiSe$_2$/CC-180 catalyst (Fig. S5). The pore size of the NiSe$_2$/CC-180 is found to be 3.8 nm and BET
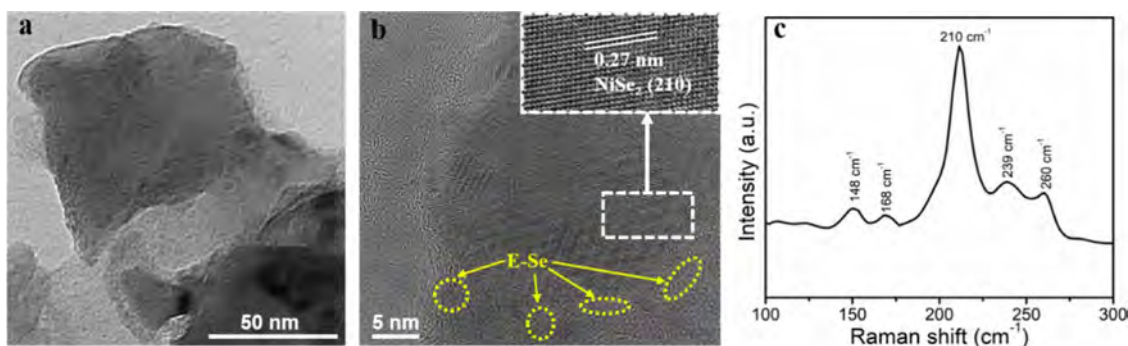
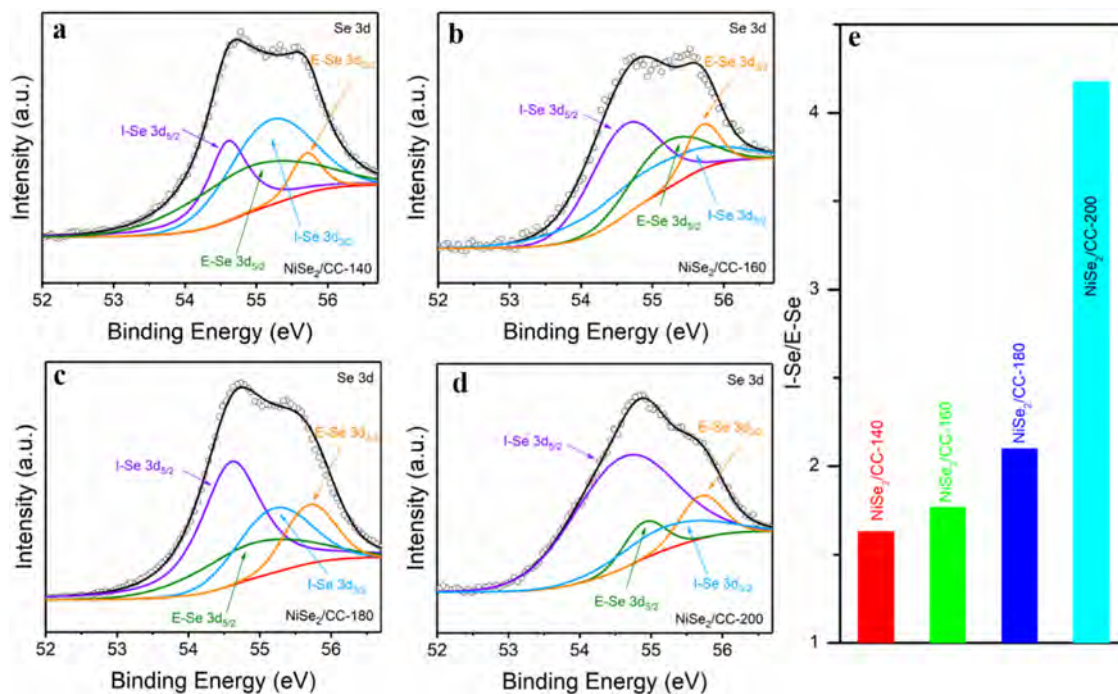**Fig. 2.** (a) TEM image, (b) HR-TEM (yellow circles showing the amorphous phase), (c) Raman scattering spectrum of NiSe$_2$/CC-180.

Fig. 3. High-resolution XPS spectra of Se 3d: (a) NiSe$_2$/CC-140, (b) NiSe$_2$/CC-160, (c) NiSe$_2$/CC-180, (d) NiSe$_2$/CC-200. I-Se represents the ionic selenium in NiSe$_2$ and E-Se represents elemental selenium adsorbed on the composite electrocatalysts. (e) Calculated ratios of I-Se/E-Se for the different samples.

specific surface area is calculated to be 10 m^2 g^{-1} based on the total mass of the CC substrate and covering catalyst. The mesoporous nature of NiSe$_2$/CC-180 increases the active sites and facilitates the charge transfer kinetics by decreasing the ion paths and improving the contact area. Raman scattering is performed to determine the composition as shown in Figs. 2(c) and S6. The two weak peaks (148 and 168 cm^{-1}) correspond to the vibration modes of T_g and E_g of dumbbell Se$_2$, whereas the two strong peaks (210 and 239 cm^{-1}) stem from the stretching modes Se-Se pairs (A_g and T_g) of NiSe$_2$ [21]. The small peak at ~260 cm^{-1} is the resonance peak of amorphous elemental Se, disclosing that the composite consists of NiSe$_2$ and amorphous elemental Se [20,26].

The surface states of the NiSe$_2$/CC-n samples are characterized by XPS. The XPS survey spectrum in Fig. S7 shows the existence of Ni, Se, C, and O, and Fig. S8 shows that the high-resolution Ni 2p spectrum has three sets of doublet peaks. The peaks with lower binding energies (853.1 eV and 870.7 eV) correspond to Ni^{2+} and the other doublet peaks correspond to the nickel oxide at the binding energy (855.5 eV and 873.6 eV). The binding energies at 859.3 eV and 878.4 eV are the standard Ni satellite peaks. XPS is performed to determine the chemical states of selenium and I-Se/E-Se ratios Fig. 3.(a–d) shows the XPS spectra of NiSe$_2$

treated hydrothermally at different temperatures. The Se 3d peak NiSe$_2$ can be deconvolved into two peaks at 54.6 eV (Se 3d$_{5/2}$) and 55.2 eV (Se 3d$_{3/2}$), which can be assigned to I-Se [19]. The peaks at higher binding energies (54.9 eV and 55.7 eV) are Se 3d$_{5/2}$ and Se 3d$_{3/2}$ of E-Se [27], thereby confirming the presence of E-Se and NiSe$_2$ in the composites. The I-Se/E-Se ratios increase with the hydrothermal temperature and as shown in Fig. 3(e) and Table S1, the I-Se/E-Se ratios can be tuned such as the higher the hydrothermal temperature, the lower is the E-Se content. Since Se sites are active sites on the transition metal selenide in electrocatalysis, coupling and interactions between I-Se and E-Se impact the performance, especially the concentration of E-Se and I-Se/E-Se ratio.

3.2. HER performance evaluation

NiSe$_2$/CC is used as the working electrodes directly to evaluate the HER performance in 1 mol L^{-1} aqueous KOH and Fig. 4(a, b) show the polarization curves and Tafel slopes of the NiSe$_2$/CC electrocatalysts. The mass loading of the Se-NiSe$_2$ composite on CC is about 5.5 mg cm^{-2} (Table S2). The pristine NiO/CC exhibits negligible HER characteristics but on the other hand, NiSe$_2$/CC show enhanced HER activity such as smaller overpotentials and Tafel slopes
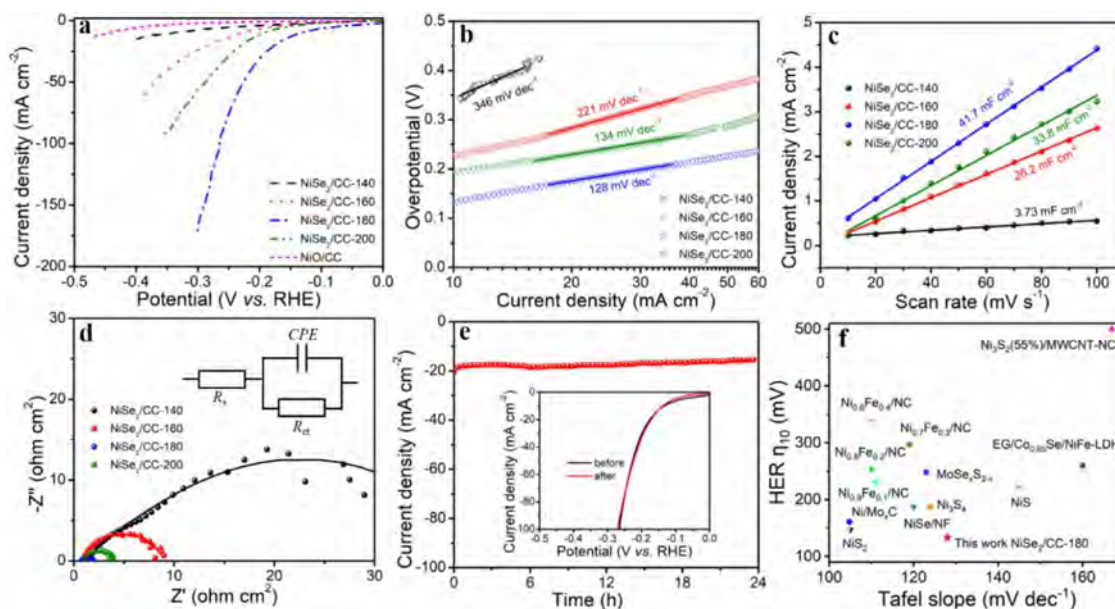
Fig. 4. Electrochemical characteristics: (a) polarization curves, (b) Tafel slopes, (c) double-layer capacitance (C_{dl}) plots, (d) Nyquist plots and corresponding circuit model; (e) Stability of the NiSe$_2$/CC-180 electrocatalyst in HER with the inset showing the polarization curves before and after cycling; (f) Comparison of the HER characteristics of recently reported electrocatalysts in 1 mol L^{-1} KOH.

due to the electrocatalytically active Se sites. As shown in Fig. 4(a), NiSe$_2$/CC-180 requires an overpotential of 133 mV to achieve a hydrogen evolution current density of 10 mA cm^{-2}, which is smaller than those of NiSe$_2$/CC-140 (352 mV), NiSe$_2$/CC-160 (235 mV), and NiSe$_2$/CC-200 (202 mV). Hence, E-Se enhances the electrocatalytic activity and the best characteristics are attained with an optimal I-Se/E-Se ratio. However, too much E-Se adsorbed on the surface may hinder exposure of active sites and so the electrocatalysts prepared at a low temperature have inferior properties. The orthorhombic phase which is less electrochemically active than the cubic phase is also associated with the poor catalytic performance at a low temperature [25].

Fig. 4(b) shows that the Tafel slope of NiSe$_2$/CC-180 (128 mV dec^{-1}) is smaller than those of NiSe$_2$/CC-140 and NiSe$_2$/CC-160 and comparable to that of NiSe$_2$/CC-200, suggesting that a large E-Se content leads to slower catalytic kinetics possibly because too much amorphous Se conceals active sites and block mass transport [25]. The HER activity depends on the electrochemical active surface area (ECSA) which is reflected by the electrochemical double-layer capacitance (C_{dl}) derived from the CV curves in the non-Faraday region, as shown in Fig. S9. Fig. 4(c) shows that C_{dl} of NiSe$_2$/CC-180 is 41.7 mF cm^{-2}, which is 11 times, 1.6 times, and 1.2 times larger than those of NiSe$_2$/CC-140 (3.73 mF cm^{-2}), NiSe$_2$/CC-160 (26.2 mF cm^{-2}), and NiSe$_2$/CC-200 (33.8 mF cm^{-2}), respectively. A larger C_{dl} implies exposure of more electrochemically active sites. With decreasing hydrothermal temperature, the I-Se/E-Se ratios decrease suggesting larger E-Se concentrations. E-Se enhances the electrocatalytic activity because an optimal amount of E-Se balances the interactions between E-Se and I-Se to achieve moderate Se-H binding and active sites exposure and produce better electrocatalytic activity. However, a large E-Se concentration on the surface decreases exposure of the active sites, slows the kinetics, and blocks mass transport. Therefore, the optimal I-Se/E-Se ratio is instrumental to the electrocatalytic performance of Se-NiSe$_2$ in order to balance the activity of the active sites and reaction kinetics.

Fig. 4(d) shows the EIS results and equivalent circuit. The electrocatalysts can be modeled by a modified equivalent circuit consisting of a series solution resistance (R_s), constant phase element (CPE), and charge transfer resistance (R_{ct}). NiSe$_2$/CC-180 has a smaller R_{ct} of ~2.6 Ω cm^2 compared to NiSe$_2$/CC-140 and NiSe$_2$/CC-160 suggesting fast kinetics. The durability of NiSe$_2$/CC-180 is evaluated by amperometry and Fig. 4(e) reveals negligible changes in the current densities after operation for 24 h at a potential of -1.35 V vs. SCE. Despite the high current density, the electrocatalyst is stable (Fig. S10) and in addition, there is no obvious change in the LSV curves before and after the stability test, indicating superior HER stability as illustrated in the inset in Fig. 4(e). Both the composition (Fig. S11) and morphology (Fig. S12) are preserved after the long stability test thus providing proof about the high physical and chemical stability of the NiSe$_2$/CC-180 electrocatalyst.

The alkaline HER characteristics of other non-precious transition metal electrocatalysts are compared and as shown in Fig. 4(f), NiSe$_2$/CC-180 shows a small overpotential for a current density of 10 mA cm^{-2}, which is superior to those of recently reported nickel/molybdenum carbide-anchored N-doped graphene/CNT hybrid (162 mV at 10 mA cm^{-2}) [28], NiSe nanowire film supported on nickel foam (187 mV at 10 mA cm^{-2}) [29], Ni$_3$S$_2$(55%)/MWCNT-NC (~500 mV at 10 mA cm^{-2}) [30], Ni^{3+} enriched nickel sulfide nanospheres (NiS, 220 mV, Ni$_3$S$_4$, 187 mV, NiS$_2$, 147 mV at 10 mA cm^{-2}) [31], cobalt selenide/NiFe layered-double-hydroxide nanosheets on exfoliated graphene (260 mV at 10 mA cm^{-2}) [32], ultrathin ternary molybdenum sulfoselenide nanosheets (248 mV at 10 mA cm^{-2}) [33], and nickel-iron/nanocarbon hybrids (Ni$_{0.9}$Fe$_{0.1}$/NC, 231 mV, Ni$_{0.8}$Fe$_{0.2}$/NC, 253 mV, Ni$_{0.7}$Fe$_{0.3}$/NC, 297 mV, Ni$_{0.6}$Fe$_{0.4}$/NC, 337 mV at 10 mA cm^{-2}) [34].

3.3. Analysis of the reaction mechanism

Density-functional theory (DFT) calculation is performed to elucidate the effects of E-Se adsorption on the HER activity of NiSe$_2$/CC under alkaline conditions. According to the previous work, the active centers are at the Se sites on NiSe$_2$ electrocatalysts [20] and the strongest XRD peak (Fig. 1(c)) and lattice (Fig. 2(b)) arise from the NiSe$_2$ (210) plane. Accordingly, the optimal model of NiSe$_2$ (210) is constructed as shown in Fig. S13. The I-Se/E-Se ratios (e.g., 1:1, 2:1, and 4:1) are determined from the number of I-Se
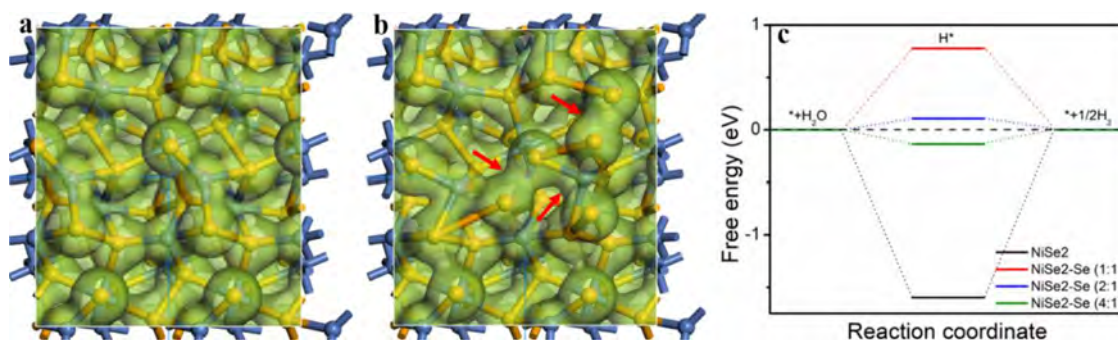
Fig. 5. Calculated charge density distributions: (a) pristine NiSe$_2$ and (b) NiSe$_2$-Se (2:1); (c) Gibbs free energy diagram for alkaline HER on the Se sites of NiSe$_2$ for different I-Se/E-Se ratios (* representing the clean surface).
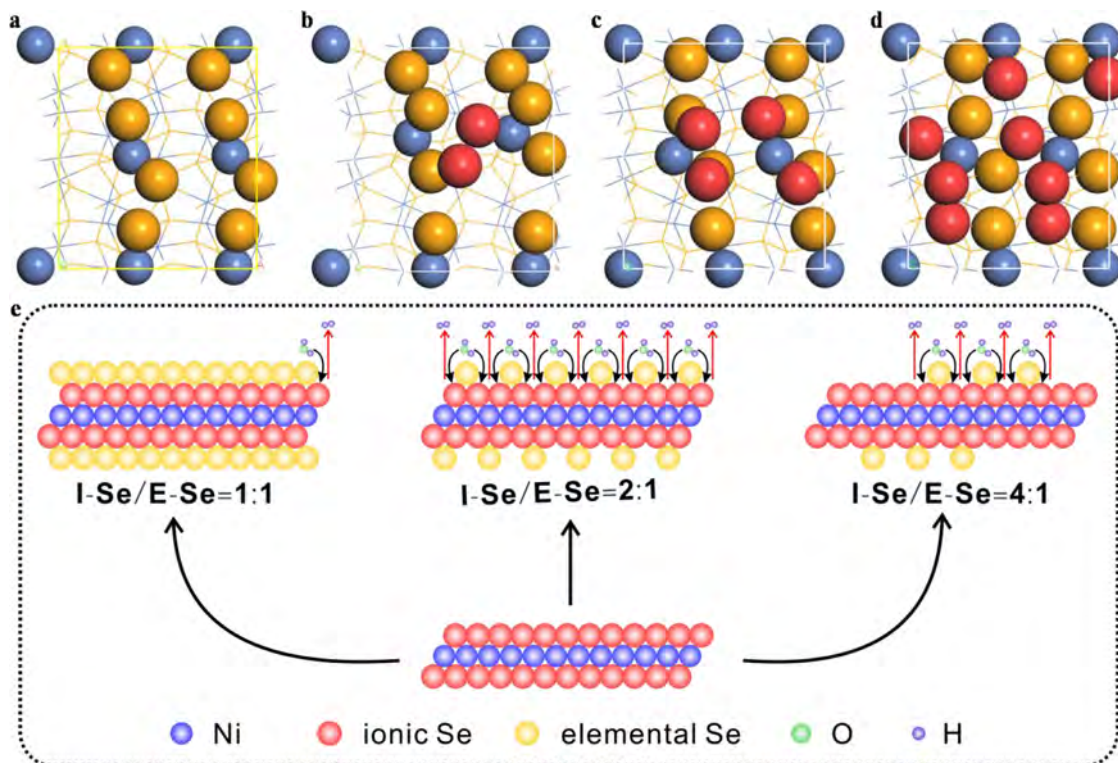

Fig. 6. Optimized surface atom distributions of the electrocatalysts with different I-Se/E-Se ratios: (a) clean NiSe$_2$, (b) NiSe$_2$-Se (4:1), (c) NiSe$_2$-Se (2:1), (d) NiSe$_2$-Se (1:1) [Red: adsorbed E-Se, brown: I-Se in NiSe$_2$, grey: Ni in NiSe$_2$]. (e) Electrocatalytic mechanism of NiSe$_2$ with different I-Se/E-Se ratios in alkaline HER.

atoms in the top layer in the model and absorbed E-Se atoms on the surface. The constructed composite is designated as NiSe$_2$-Se (*m:n*), where *m:n* represents the I-Se/E-Se ratio. Compared to pristine NiSe$_2$, the higher charge density of the NiSe$_2$-Se electrocatalysts, particularly the E-Se and I-Se, E-Se and E-Se regions (pointed by red arrows), reveals an improved electron environment for electrocatalytic water splitting, as illustrated in Figs. 5(a, b) and S14. Additionally, the density of states (DOS) results in Fig. S15 uncover that the NiSe$_2$-Se electrocatalysts have higher states in the region close to the Fermi level, and the more the adsorbed E-Se, the stronger the DOS. However, a stronger DOS may not give rise to a higher electrochemical activity, since some charge densities come from the interactions between the adsorbed E-Se themselves (Figs. 5(b) and S14) and may not contribute to electrocatalysis.

Alkaline HER occurs via two sequential steps including the Volmer step (water dissociation to break the H-O bond and form adsorbed H* intermediates) and Tafel step (release of adsorbed H* to produce H$_2$) [35]. The adsorption free energies of H* are calculated and as shown in Fig. 5(c), vary significantly compared to the

clean NiSe$_2$ surface. Generally, an ideal HER electrocatalyst should have a ΔG_{H*} close to zero for moderate H adsorption and desorption [36]. A larger ΔG_{H*} implies that strong Se-H bonding at the clean NiSe$_2$ surface is weakened after E-Se adsorption. As a result, ΔG_{H*} follows the order of NiSe$_2$-Se (2:1) < NiSe$_2$-Se (4:1) < NiSe$_2$-Se (1:1), suggesting that the NiSe$_2$-Se (2:1) surface is the most suitable for H adsorption and desorption.

The results reveal that E-Se adsorption on NiSe$_2$ weakens Se-H bonding during HER. The more the amount of adsorbed E-Se, the weaker the Se-H binding and the larger the atomic density of E-Se at the surface, as shown in Fig. 6(a–d) and schematically illustrated in Fig. 6(e). Although weak Se-H binding can ease gas release, weak binding compromises adsorption of H* intermediates affecting mass transport. Generally, too much E-Se on the surface hides the active sites (Fig. 6(e), left) resulting in sharp decay in the ECSA, as shown in Fig. 4(c). An optimal amount of E-Se balances the interactions between E-Se and I-Se to achieve moderate Se-H binding and active sites exposure leading to the best electrocatalytic activity (Fig. 6(e), middle).
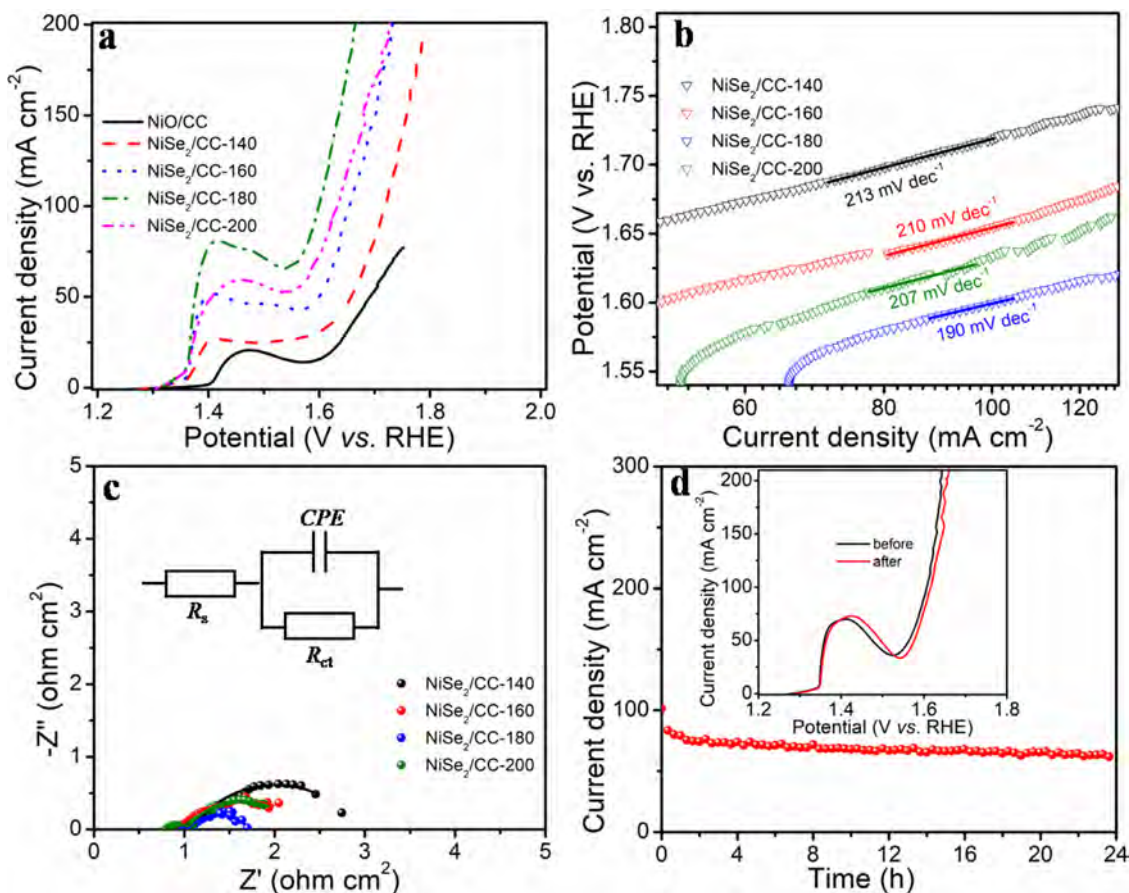
Fig. 7. OER performance of the electrocatalysts in 1 mol L^{-1} KOH aqueous solution: (a) polarization curves, (b) Tafel slopes, (c) Nyquist plots and corresponding circuit of the electrocatalysts, (d) stability of the NiSe$_2$/CC-180 electrocatalyst in OER with inset showing the polarization curves before and after cycling.
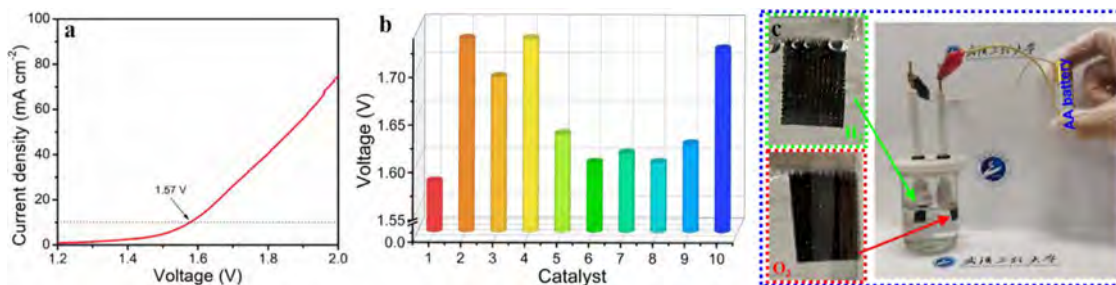

Fig. 8. (a) Overall water splitting characteristics of the device with NiSe$_2$/CC-180 as both the anode and cathode; (b) Comparison of the voltage required to generate a current density of 10 mA cm^{-2} in overall water splitting with those of recently reported non-precious transition metal electrocatalyst couples: (1) NiSe$_2$/CC-180 in this work, (2) FeSe$_2$/NF [39], (3) Ultra-thin non-layered NiSe [40], (4) Ni$_{0.5}$Se-OER//Ni$_{0.75}$Se-HER [41], (5) NiSe/NF [29], (6) Co$_7$Se$_8$ nanostructures [42], (7) Ni$_3$Se$_2$/NiSe [43], (8) 3D Se-(NiCo)S$_x$/(OH)$_x$ nanosheets [44], (9) Ni-Co-P hollow nanobricks [45], (10) Co(OH)$_2$@NCNTs@NF [46]; (c) Photo of the water splitting system powered by an AA battery.

Based on the above discussion, the NiSe$_2$/CC-*n* samples show better HER activity due to the following reasons:

(1) Structurally, the porous nano-sheet structure has a larger specific surface area, which can provide more active sites, that is, increase the non-intrinsic activity, and appropriate Se adsorption on NiSe$_2$ surface can provide more active sites.
(2) As for the electrical conductivity, the carbon cloth substrate has a certain electrical conductivity and the catalyst has high charge transfer efficiency. The synergistic effects between selenium-rich components on the surface and nickel selenide promote the acceleration of the kinetics.
(3) In terms of the catalytic performance, it is important that the appropriate I-Se/E-Se ratio plays an important role in the elec-

trocatalytic performance of NiSe$_2$ in order to balance the catalytic activity and reaction kinetics.

3.4. OER performance evaluation

It is important to evaluate the OER performance of the NiSe$_2$ in the context of the development of multifunctional catalysts for overall water splitting. The OER characteristics of NiSe$_2$/CC are investigated, as shown in Fig. 7. Prior to water oxidation, oxidation of nickel selenide occurs at 1.4–1.5 V (vs. RHE), which severely obscures the early OER signal and makes it difficult to determine the overpotential at a current density of 10 mA cm^{-2} including the starting potential in OER similar to the literature [37,38]. As shown in Fig. 7(a), NiSe$_2$/CC-180 requires a potential of 1.58 V vs. RHE to achieve a current density of 100 mA cm^{-2}, which is smaller than

those of NiSe$_2$/CC-140 (1.828 V vs. RHE), NiSe$_2$/CC-160 (1.747 V vs. RHE), NiSe$_2$/CC-200 (1.63 V vs. RHE), and other nickel and selenide electrocatalysts listed in Table S3. The results confirm that the I-Se/E-Se ratio plays a significant role in OER as well Fig. 7(b) shows that NiSe$_2$/CC-180 has the smallest Tafel slope of 190 mV dec^{-1}, which is consistent with the smallest charge transfer resistance in the Nyquist plots in Fig. 7(c). The Tafel slopes of these electrocatalysts are larger than those reported earlier due to the large current density (as high as ∼80 mA cm^{-2}) of the oxidation peaks making the onset potential in OER difficult to define. NiSe$_2$/CC-180 exhibits excellent stability in OER because the current density of 75 mA cm^{-2} is maintained for 24 h during continuous testing under alkaline conditions, as shown in Fig. 7(d). Moreover, the overpotential shifts by only 8 mV at the current density of 100 mA cm^{-2} after the long-term stability test, as revealed by the inset in Fig. 7(d).

3.5. Overall water splitting performance

Since NiSe$_2$/CC-180 has superior HER and OER characteristics, an overall water splitting device with NiSe$_2$/CC-180 as both the anode and cathode being assembled with 1 mol L^{-1} KOH as the electrolyte. As shown in Fig. 8(a), to deliver a current density of 10 mA cm^{-2}, the potential is only 1.57 V, which is better than those of many non-precious transition metal electrocatalyst couples, as shown in Fig. 8(b) and Table S4. To demonstrate the commercial potential, the overall water splitting system can be powered by an AA battery (1.5 V) and hydrogen and oxygen generation are observed as shown in Fig. 8(c).

4. Conclusion

Se-NiSe$_2$ hybrid nanosheets with adsorbed amorphous E-Se are prepared on CC by a solution technique and hydrothermal method and the I-Se/E-Se ratio can be adjusted by the hydrothermal temperature. The NiSe$_2$/CC electrocatalyst exhibits excellent electrochemical activity due to the two-dimensional nanosheet arrays, large electrochemical surface area, and good electrical conductivity. The amount of adsorbed amorphous (E-Se) plays a significant role in the electrocatalytic characteristics and the optimal I-Se/E-Se ratio leads to better electrocatalytic activity and reaction kinetics in both HER and OER. As a result, NiSe$_2$/CC-180 requires overpotentials of only 133 mV to generate a hydrogen evolution current density of 10 mA cm^{-2} and 350 mV to generate an oxygen evolution current density of 100 mA cm^{-2}. The overall water splitting device constructed with the bifunctional NiSe$_2$/CC-180 electrodes requires 1.57 V to produce a current density of 10 mA cm^{-2}. The results enrich our fundamental knowledge about the reaction mechanisms of transition metal selenides in water splitting and provide insights into the design and development of efficient non-noble metal electrocatalysts.

Acknowledgments

Supplementary materials

Supplementary material associated with this article can be found, in the online version, at doi:10.1016/j.jmst.2021.12.022.

References

[1] I. Roger, M.A. Shipman, M.D. Symes, Nat. Rev. Chem. 1 (2017) 0003.
[2] V.R. Stamenkovic, D. Strmcnik, P.P. Lopes, N.M. Markovic, Nat. Mater. 16 (2017) 57–69.
[3] X. Zou, Y. Zhang, Chem. Soc. Rev. 44 (2015) 5148–5180.
[4] X. Peng, L. Wang, L. Hu, Y. Li, B. Gao, H. Song, C. Huang, X. Zhang, J. Fu, K. Huo, P.K. Chu, Nano Energy 34 (2017) 1–7.
[5] X. Peng, C. Pi, X. Zhang, S. Li, K. Huo, P.K. Chu, Sustain. Energy Fuels 3 (2019) 366–381.
[6] R. Hao, Q.L. Feng, X.J. Wang, Y.C. Zhang, K.S. Li, Rare Met. 41 (2022) 1314–1322.
[7] X. Peng, X. Jin, B. Gao, Z. Liu, P.K. Chu, J. Catal. 398 (2021) 54–66.
[8] X.J. Fang, L.P. Ren, F. Li, Z.X. Jiang, Z.G. Wang, Rare Met. 41 (2022) 901–910.
[9] K. Jiang, B. Liu, M. Luo, S. Ning, M. Peng, Y. Zhao, Y.R. Lu, T.S. Chan, F.M.F. de Groot, Y. Tan, Nat. Commun. 10 (2019) 1743.
[10] X. Peng, A.M. Qasim, W. Jin, L. Wang, L. Hu, Y. Miao, W. Li, Y. Li, Z. Liu, K. Huo, K.Y. Wong, P.K. Chu, Nano Energy 53 (2018) 66–73.
[11] X. Peng, L. Hu, L. Wang, X. Zhang, J. Fu, K. Huo, L.Y.S. Lee, K.Y. Wong, P.K. Chu, Nano Energy 26 (2016) 603–609.
[12] X. Peng, X. Jin, N. Liu, P. Wang, Z. Liu, B. Gao, L. Hu, P.K. Chu, Appl. Surf. Sci. 567 (2021) 150779.
[13] S. Han, Y.C. Pu, L. Zheng, L. Hu, J.Z. Zhang, X. Fang, J. Mater. Chem. A 4 (2016) 1078–1086.
[14] X.X. Li, P.Y. Zhu, Q. Li, Y.X. Xu, Y. Zhao, H. Pang, Rare Met. 39 (2020) 680–687.
[15] W.L. Ding, Y.H. Cao, H. Liu, A.X. Wang, C.J. Zhang, X.R. Zheng, Rare Met. 40 (2021) 1373–1382.
[16] Y. Huang, J. Ren, X. Qu, Chem. Rev. 119 (2019) 4357–4412.
[17] X. Peng, Y. Yan, X. Jin, C. Huang, W. Jin, B. Gao, P.K. Chu, Nano Energy 78 (2020) 105234.
[18] Y. Sun, K. Xu, Z. Wei, H. Li, T. Zhang, X. Li, W. Cai, J. Ma, H.J. Fan, Y. Li, Adv. Mater. 30 (2018) 1802121.
[19] J. Liang, Y. Yang, J. Zhang, J. Wu, P. Dong, J. Yuan, G. Zhang, J. Lou, Nanoscale 7 (2015) 14813–14816.
[20] F. Wang, Y. Li, T.A. Shifa, K. Liu, F. Wang, Z. Wang, P. Xu, Q. Wang, J. He, Angew. Chem. Int. Ed. 55 (2016) 6919–6924.
[21] H. Zhou, F. Yu, Y. Liu, J. Sun, Z. Zhu, R. He, J. Bao, W.A. Goddard, S. Chen, Z. Ren, Energy Environ. Sci. 10 (2017) 1487–1492.
[22] W. Zhao, C. Zhang, F. Geng, S. Zhuo, B. Zhang, ACS Nano 8 (2014) 10909–10919.
[23] X.H. Xia, J.P. Tu, J. Zhang, X.L. Wang, W.K. Zhang, H. Huang, Sol. Energy Mater. Sol. Cells 92 (2008) 628–633.
[24] R. Liu, X. Peng, X. Han, C.H. Mak, K.C. Cheng, S.P. Santoso, H.H. Shen, Q. Ruan, F. Cao, T.Y. Edward, J. Electroanal. Chem. 887 (2021) 115167.
[25] J. Zhou, Y. Liu, Z. Zhang, Z. Huang, X. Chen, X. Ren, L. Ren, X. Qi, J. Zhong, Electrochim. Acta 279 (2018) 195–203.
[26] L. Liu, Q. Peng, Y. Li, Nano Res. 1 (2008) 403–411.
[27] C. Zhang, H. Tao, Y. Dai, X. He, K. Zhang, Prog. Nat. Sci. 24 (2014) 671–675.
[28] D. Das, S. Santra, K.K. Nanda, ACS Appl. Mater. Interfaces 10 (2018) 35025–35038.
[29] C. Tang, N. Cheng, Z. Pu, W. Xing, X. Sun, Angew. Chem. Int. Ed. 54 (2015) 9351–9355.
[30] T.W. Lin, C.J. Liu, C.S. Dai, Appl. Catal. B Environ. 154-155 (2014) 213–220.
[31] X. Shi, X. Ling, L. Li, C. Zhong, Y. Deng, X. Han, W. Hu, J. Mater. Chem. A 7 (2019) 23787–23793.
[32] G.W. Tang, Q. Qian, K.L. Peng, X. Wen, G.X. Zhou, M. Sun, X.D. Chen, Z.M. Yang, AIP Adv. 5 (2015) 027113.
[33] J. Si, H. Chen, C. Lei, Y. Suo, B. Yang, Z. Zhang, Z. Li, L. Lei, J. Chen, Y. Hou, Nanoscale 11 (2019) 16200–16207.
[34] X. Zhang, H. Xu, X. Li, Y. Li, T. Yang, Y. Liang, ACS Catal. 6 (2016) 580–588.
[35] H. Zhang, X. Wu, C. Chen, C. Lv, H. Liu, Y. Lv, J. Guo, J. Li, D. Jia, F. Tong, Chem. Eng. J. (2020) 128069.
[36] C. Huang, X. Miao, C. Pi, B. Gao, X. Zhang, P. Qin, K. Huo, X. Peng, P.K. Chu, Nano Energy 60 (2019) 520–526.
[37] J. Zhang, Y. Wang, C. Zhang, H. Gao, L. Lv, L. Han, Z. Zhang, ACS Sustain. Chem. Eng. 6 (2018) 2231–2239.
[38] P. Wang, Z. Pu, W. Li, J. Zhu, C. Zhang, Y. Zhao, S. Mu, J. Catal. 377 (2019) 600–608.
[39] C. Panda, P.W. Menezes, C. Walter, S. Yao, M.E. Miehlich, V. Gutkin, K. Meyer, M. Driess, Angew. Chem. Int. Ed. 56 (2017) 10506–10510.
[40] H. Wu, X. Lu, G. Zheng, G.W. Ho, Adv. Energy Mater. 8 (2018) 1702704.
[41] X. Zheng, X. Han, H. Liu, J. Chen, D. Fu, J. Wang, C. Zhong, Y. Deng, W. Hu, ACS Appl. Mater. Interfaces 10 (2018) 13675–13684.
[42] J. Masud, A.T. Swesi, W.P. Liyanage, M. Nath, ACS Appl. Mater. Interfaces 8 (2016) 17292–17302.
[43] Y. Zhong, B. Chang, Y. Shao, C. Xu, Y. Wu, X. Hao, ChemSusChem 12 (2019) 2008–2014.
[44] C. Hu, L. Zhang, Z.J. Zhao, A. Li, X. Chang, J. Gong, Adv. Mater. 30 (2018) 1705538.
[45] Y. Chen, S. Ji, C. Chen, Q. Peng, D. Wang, Y. Li, Joule 2 (2018) 1242–1264.
[46] P. Guo, J. Wu, X.B. Li, J. Luo, W.M. Lau, H. Liu, X.L. Sun, L.M. Liu, Nano Energy 47 (2018) 96–104.

Supplementary Information

Se-NiSe₂ hybrid nanosheet arrays with self-regulated elemental Se for efficient alkaline water splitting

Xiang Peng[a, b], Yujiao Yan[a], Shijian Xiong[a], Yaping Miao[c], Jing Wen[a], Zhitian Liu[a, *], Biao Gao[b,d,*], Liangsheng Hu[e], Paul K. Chu[b,*]

[a] Hubei Key Laboratory of Plasma Chemistry and Advanced Materials, Hubei Engineering Technology Research Center of Optoelectronic and New Energy Materials, Wuhan Institute of Technology, Wuhan 430205, China

[b] Department of Physics, Department of Materials Science and Engineering, Department of Biomedical Engineering, City University of Hong Kong, Tat Chee Avenue, Kowloon, Hong Kong, China

[c] School of Textile Science and Engineering, Xi'an Polytechnic University, Xi'an 710048, China

[d] State Key Laboratory of Refractories and Metallurgy and Institute of Advanced Materials and Nanotechnology, Wuhan University of Science and Technology, Wuhan 430081, China

[e] Department of Chemistry and Key Laboratory for Preparation and Application of Ordered Structural Materials of Guangdong Province, Shantou University, Shantou 515063, China
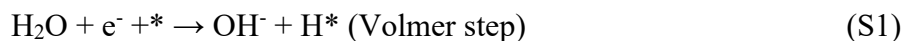
*Corresponding authors.

E-mail addresses: able.ztliu@wit.edu.cn (Z. Liu); gaobiao@wust.edu.cn (B. Gao);

paul.chu@cityu.edu.hk (Paul K. Chu).

Calculation method

The density-functional theory (DFT) calculation was performed using the DMol3 program implemented in Material Studio [1] and the slab model with a vacuum space of 15 Å along the z-direction was adopted for NiSe$_2$. The (210) surface was selected in the models due to the strongest diffraction signal in the XRD pattern and lattice revealed by HR-TEM. The exchange-correlation functional under the generalized gradient approximation (GGA) within the Perdew-Burke-Ernzerhof (PBE) functional was implemented [2]. The core electrons were treated with DFT semi-core pseudopotentials (DSPPs) and the TS method was employed to correct for dispersion [3, 4]. The atoms in the bottom layer were fixed to simulate support and others were relaxed to simulate the reactive surface of the catalysts. The ratio of ionic Se to elemental Se was determined from the number of Se atoms in the top layer and Se atoms adsorbed on the surface. Based on previous studies, the mechanism of HER in alkaline media can be described as shown in the following:

$$H_2O + e^- + * \rightarrow OH^- + H* \text{ (Volmer step)} \quad\quad\quad\quad (S1)$$

$$H* + H* \rightarrow H_2 + 2* \text{ (Tafel step)} \hspace{4cm} \text{(S2)}$$

where * denotes the clean electrocatalyst surface. The adsorption energy ΔE of the H atoms on the surface of the substrate is defined as:

$$\Delta E = E_{*H} - (E_* + E_H) \hspace{4cm} \text{(S3)}$$

where *H and * denote adsorbed H atoms on the sample and bare substrate, and E_H denotes the half of energy of H_2 [5].

The adsorption free energy change ΔG in the reaction was calculated as the difference between the free energies of the initial and final states as shown below:

$$\Delta G = \Delta E + \Delta ZPE - T\Delta S \hspace{4cm} \text{(S4)}$$

where E, ZPE, and TS are the energy derived by DFT, zero-point energy correction, and entropy correction, respectively. The correction data for the zero-point energy and entropy of the gaseous and adsorbed species can be found in the literature [6].
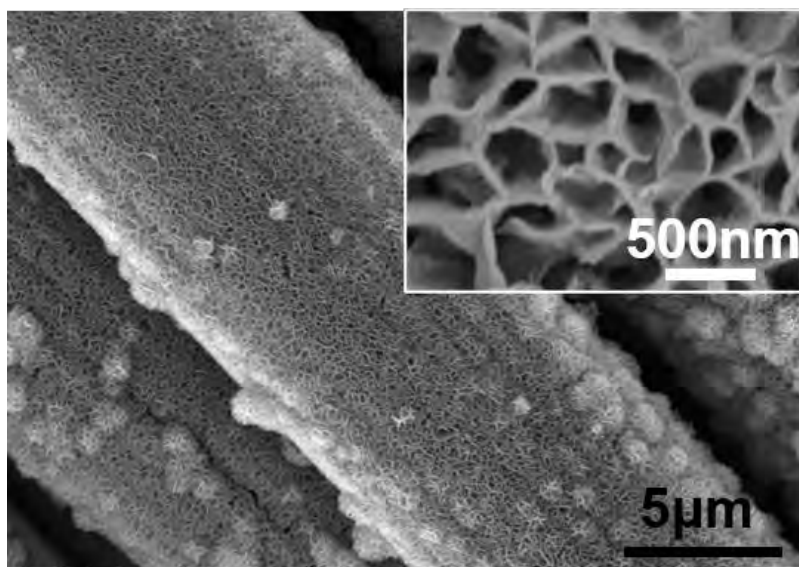
Fig. S1. SEM image of the hydrothermal product (NiOH/Ni(OH)$_2$/CC) with the high-

magnification image shown in the inset.
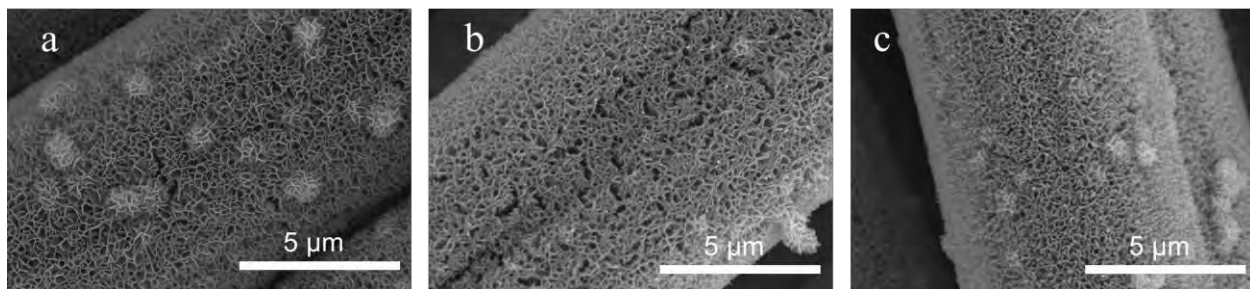
Fig. S2. SEM images: (a) NiSe$_2$/CC-140, (b) NiSe$_2$/CC-160, (c) NiSe$_2$/CC-200.
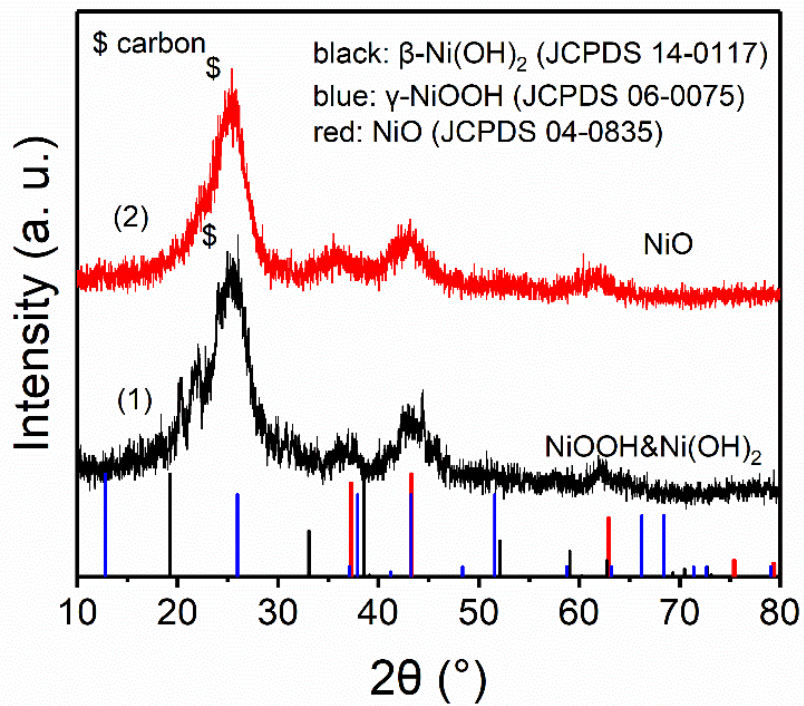
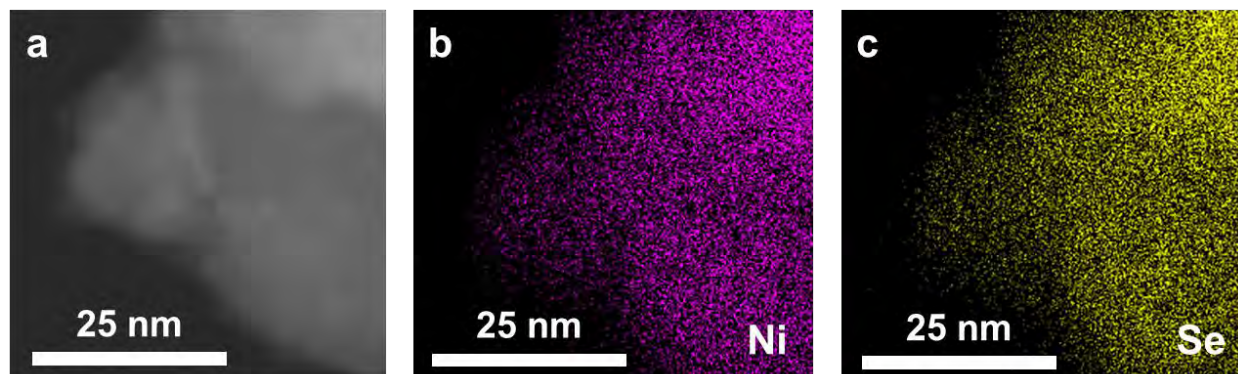**Fig. S3.** XPD patterns of the hydrothermal and annealed products.

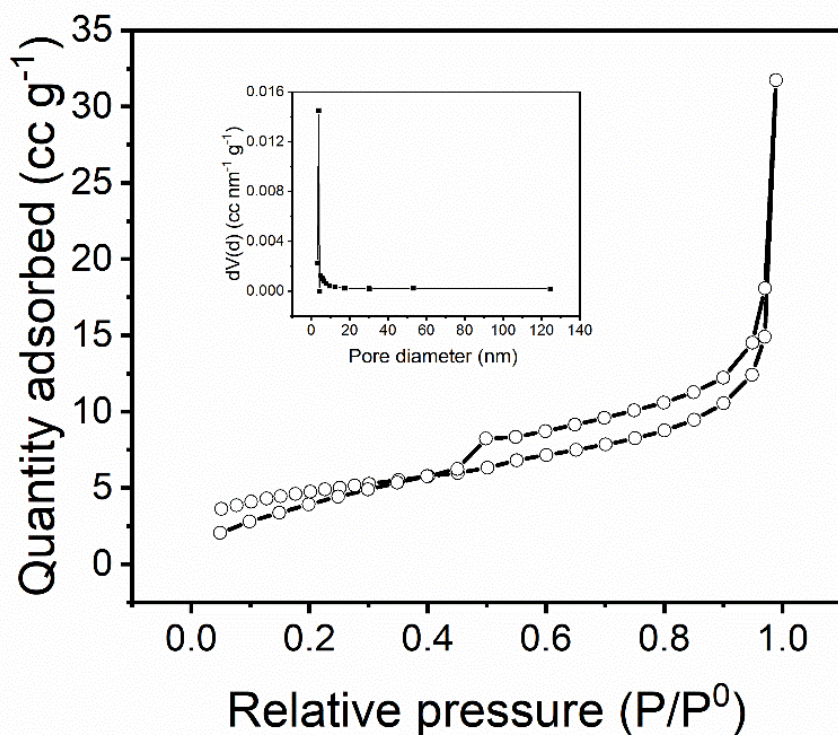**Fig. S4.** Elemental maps of the NiSe$_2$/CC-180 electrocatalyst.

Fig. S5. Nitrogen adsorption-desorption isotherms and pore-size distributions of the NiSe$_2$/CC-180 electrocatalyst.
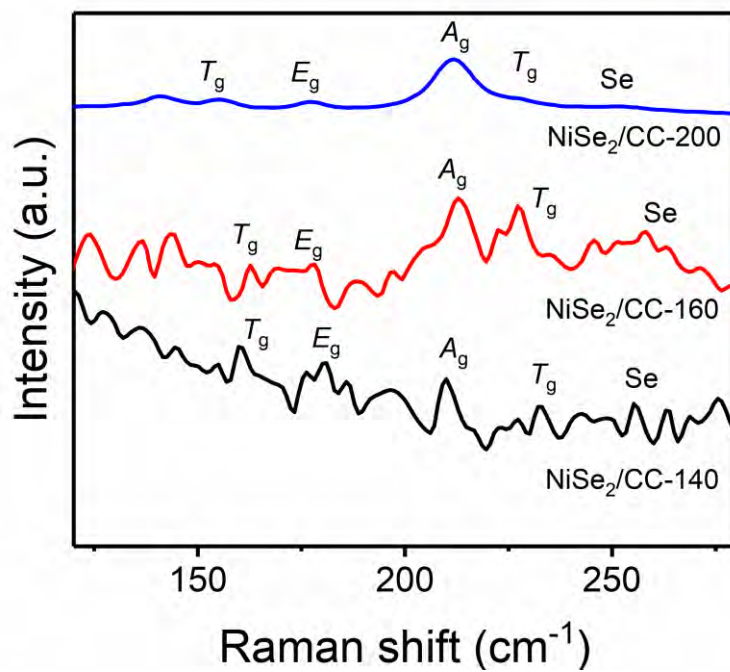
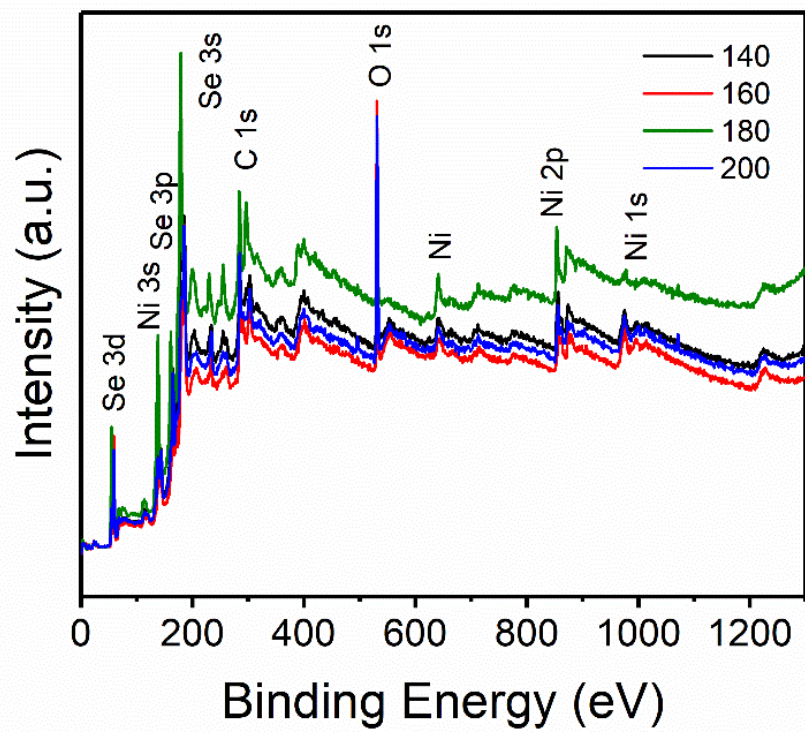**Fig. S6.** Raman scattering spectra of NiSe$_2$/CC-140, NiSe$_2$/CC-160, and NiSe$_2$/CC-200.

Fig. S7. XPS survey spectra of NiSe$_2$/CC-140, NiSe$_2$/CC-160, NiSe$_2$/CC-180, and NiSe$_2$/CC-200.
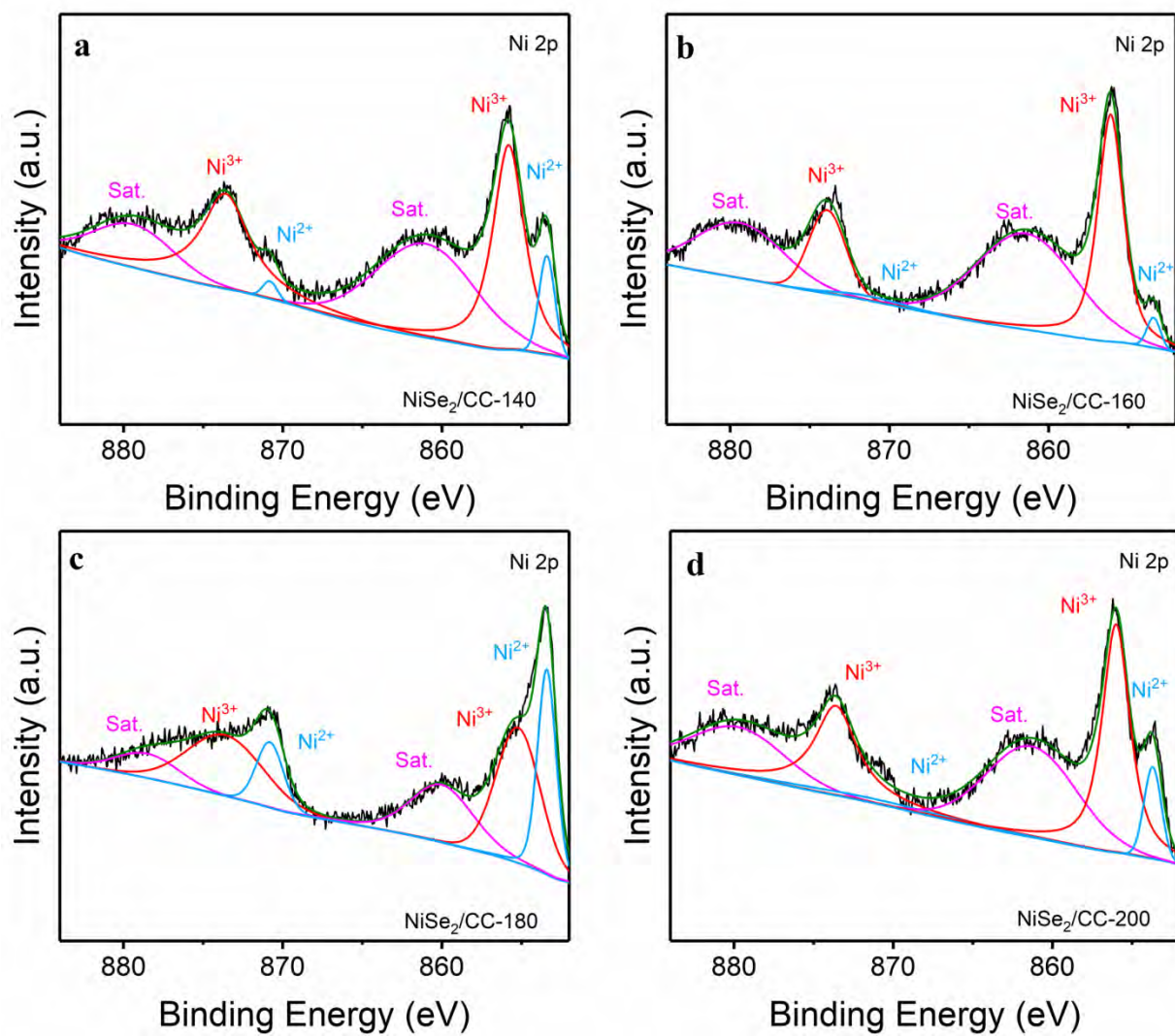
Fig. S8. High-resolution XPS Ni 2p spectra: (a) NiSe$_2$/CC-140, (b) NiSe$_2$/CC-160, (c) NiSe$_2$/CC-180, (d) NiSe$_2$/CC-200.

Table S1 Ratios of I-Se/E-Se acquired by XPS from the samples treated hydrothermally at

different temperatures.

Samples	I-Se/E-Se ratios
NiSe$_2$/CC-140	1.63
NiSe$_2$/CC-160	1.77
NiSe$_2$/CC-180	2.10
NiSe$_2$/CC-200	4.18

Table S2 Mass loadings of the samples hydrothermally treated at different temperatures.

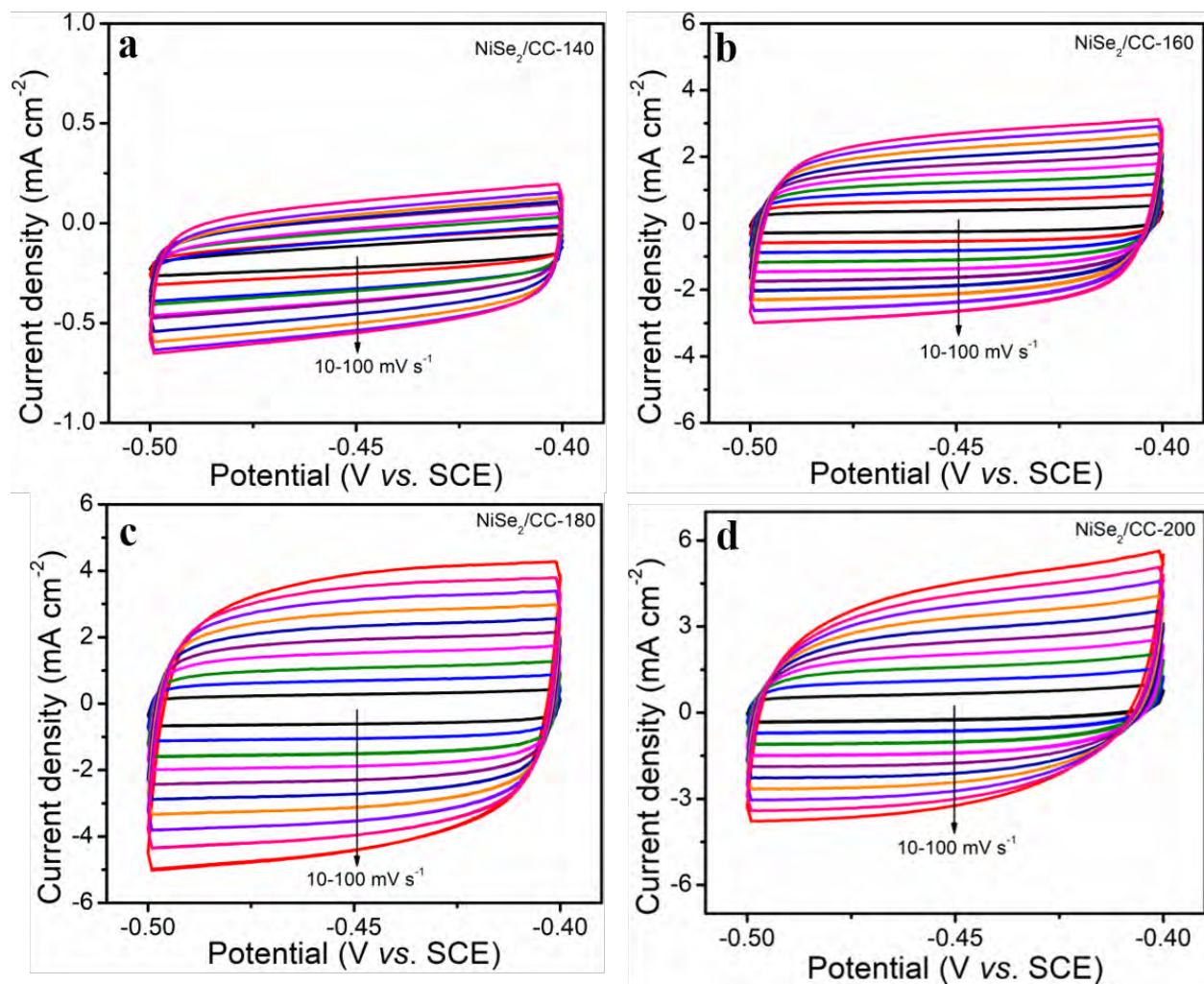| Samples	Mass loadings (mg cm^{-2})
NiSe$_2$/CC-140	5.75
NiSe$_2$/CC-160	5.58
NiSe$_2$/CC-180	5.57
NiSe$_2$/CC-200	5.33

Fig. S9. Electrochemical active surface areas (ECSA) determined by the double-layer capacitance (CDL) measurements using cyclic voltammetry (CV) in 1 mol/L KOH: (a) $NiSe_2$/CC-140, (b) $NiSe_2$/CC-160, (c) $NiSe_2$/CC-180, (d) $NiSe_2$/CC-200.
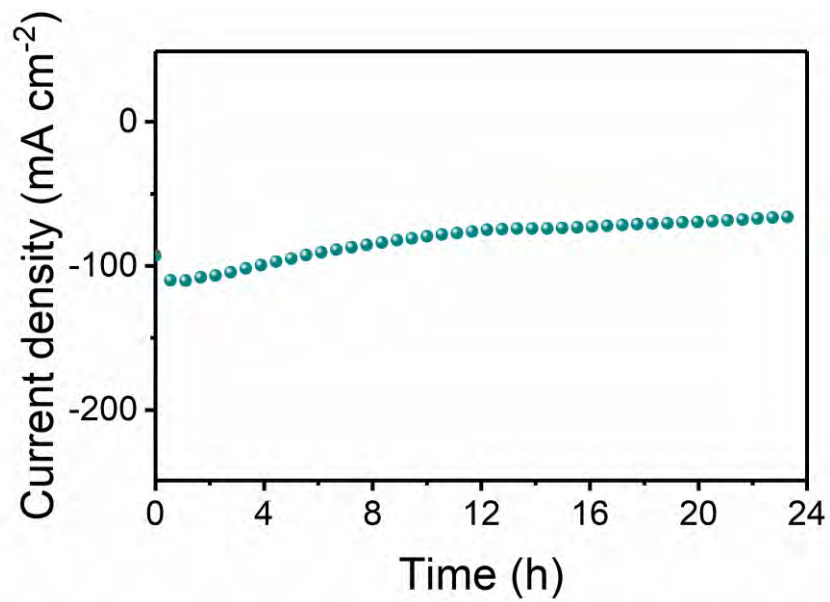
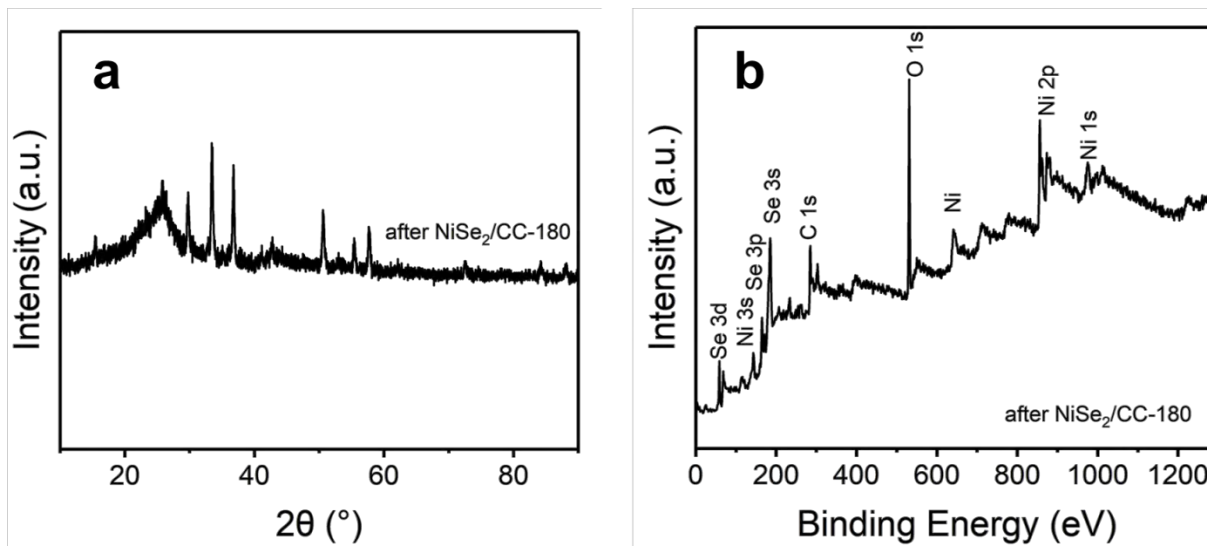**Fig. S10.** Chronoamperometric curve of NiSe$_2$/CC-180 at a high current density.

Fig. S11. Characterization after the long-term stability test of the NiSe$_2$/CC-180 electrocatalyst: (a)
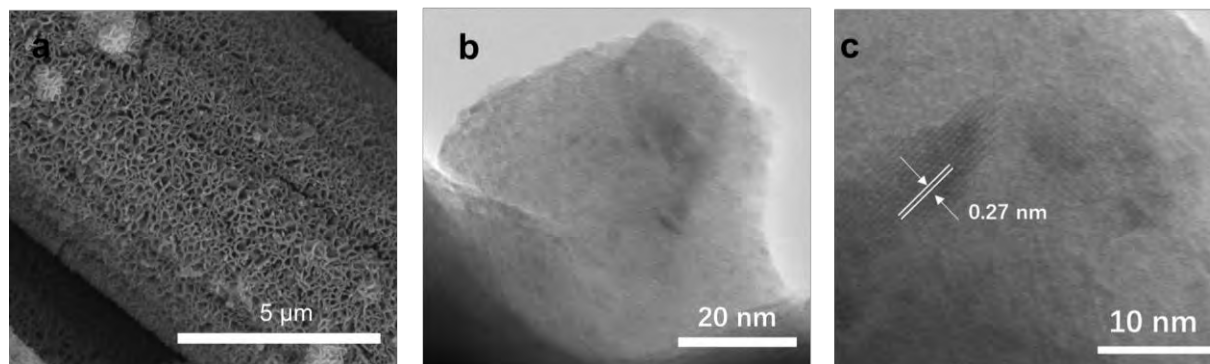
XRD, (b) XPS.

Fig. S12. Characterization after the long-term stability test of the NiSe$_2$/CC-180 electrocatalyst:
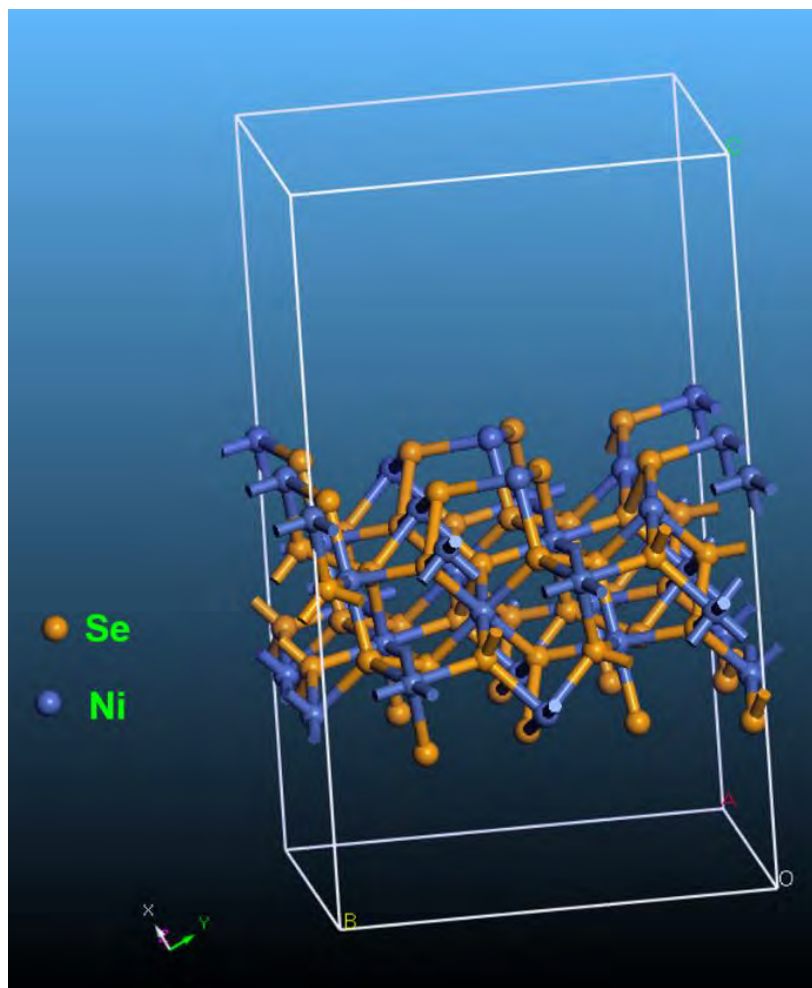
(a) SEM, (b) TEM, (c) HR-TEM.

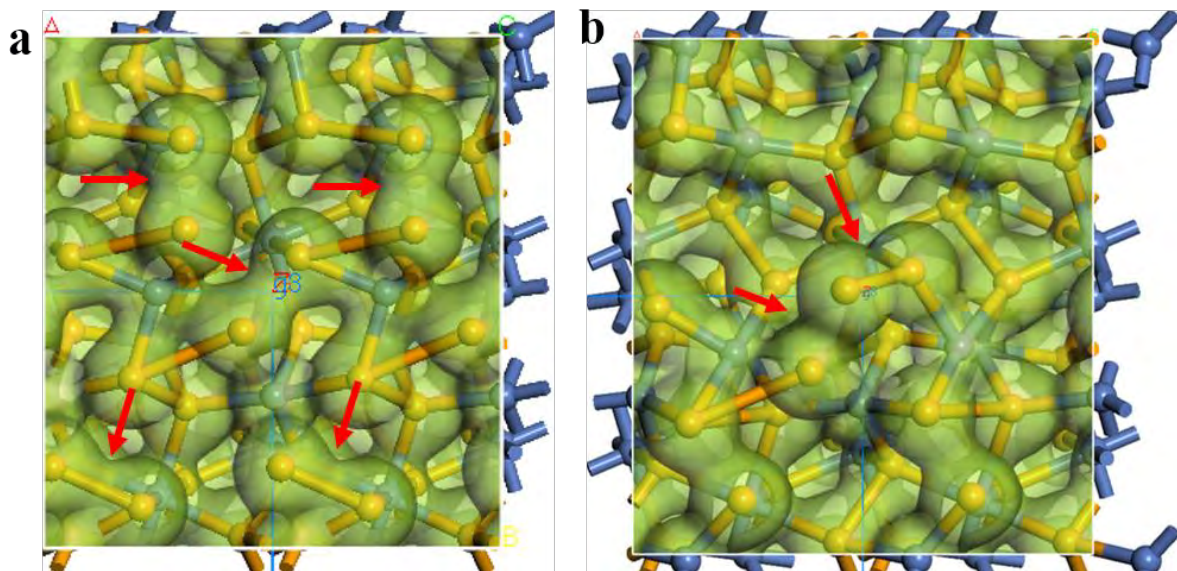**Fig. S13.** Slab model of NiSe$_2$ (210) for the DFT calculation.

Fig. S14. Calculated charge density distributions (a) $NiSe_2$-Se (1:1) and (b) $NiSe_2$-Se (4:1).
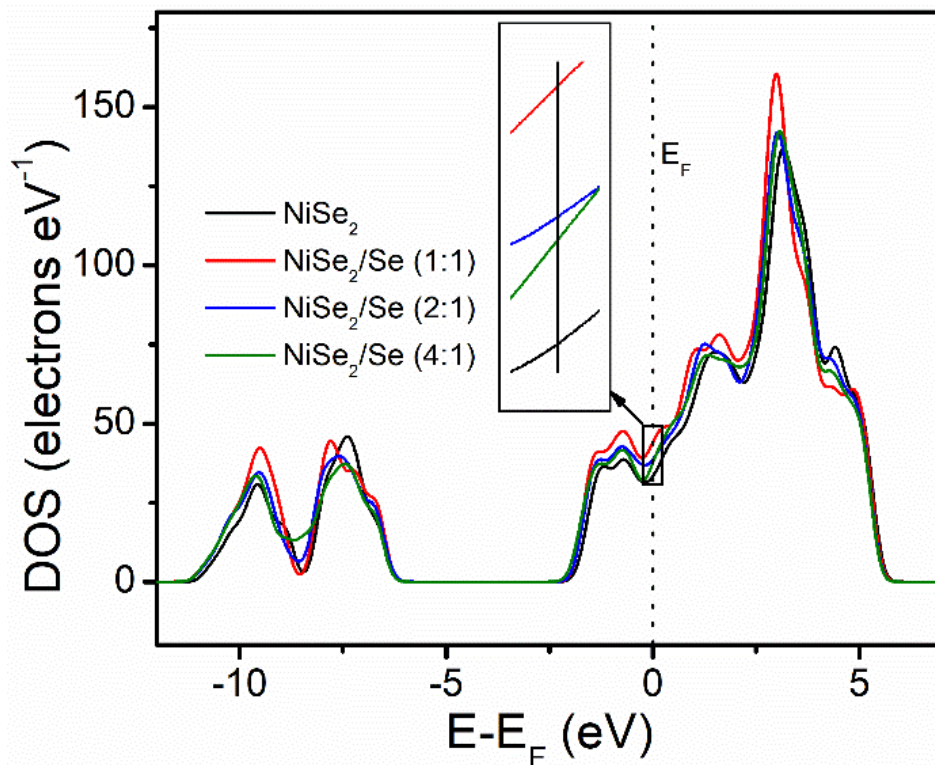
Fig. S15. Calculated total densities of states of $NiSe_2$, $NiSe_2$-Se (1:1), $NiSe_2$-Se (2:1), and $NiSe_2$-

Se (4:1) with the Fermi level aligned at 0 eV. The inset shows the magnified curves at the Fermi

level.

Table S3 Comparison of the OER characteristics of different electrocatalysts.

Catalysts	Electrolytes	η_{100} (mV)	Tafel slope (mV dec^{-1})	Morphology	Electrode structure	Refs.
FeSe$_2$ nanoplatelets	1 mol/L KOH	>500	48.1	nanoplatelets	on nickel piece	[7]
Ni$_{0.5}$Se nanocrystal	1 mol/L KOH	330@ 10 mA cm^{-2}	51	nanocrystals	on carbon paper	[8]
Ni-Co-Se/CFP	1 mol/L KOH	≈410	87	dodecahedral nanocages	on carbon fiber paper	[9]
NiSe/NF-4	1 mol/L KOH	370	95.3	nanorods nanoparticles	on Ni foam	[10]
NiSe/NF	1 mol/L KOH	411	59.4	-	on Ni foam	[11]
NiCo hydroxide nanocages	1 mol/L KOH	350@ 10 mA cm^{-2}	65	nanocages	on glassy carbon rotating disk electrode	[12]

NiFe LDH/graphitic mesoporous carbon	1 mol/L KOH	≈400	57	ordered mesoporous structure	on graphitic mesoporous carbon on rotating ring-disk glass-carbon	[13]
CoNi-SAs/NC	0.1 mol/L KOH	340@ 10 mA cm^{-2}	58.7	nanoparticles	on glassy carbon rotating ring disc electrode	[14]
Fe-NiNC	1 mol/L KOH	340@ 10 mA cm^{-2}	54	hollow spheres		[15]
NiSe$_2$/CC-180	1 mol/L KOH	350	191.08	nanosheets	on carbon cloth	this work

Table S4 Comparison of the overall water splitting characteristics of reported non-precious transition metal-based electrocatalyst couples.

Electrocatalysts	Electrolytes	V_{10} [a] (V)	Morphology	Electrode structure	Refs.
FeSe$_2$/NF	1 mol/L KOH	1.73	-	on GCE	[16]
ultra-thin non-layered NiSe	1 mol/L NaOH	1.69	ultrathin nanosheets	on Ni foam	[17]
Ni$_{0.5}$Se//Ni$_{0.75}$Se	1 mol/L KOH	1.73	nanocrystals	on carbon paper	[8]
NiSe/NF	1 mol/L KOH	1.63	nanowire film	on Ni foam	[18]
Co$_7$Se$_8$ nanostructures	1 mol/L KOH	1.60	film	on GCE	[19]
Ni$_3$Se$_2$/NiSe	1 mol/L KOH	1.61	nanorods nanoparticles	on Ni foam	[10]
3D Se-(NiCo)S$_x$/(OH)$_x$ nanosheets	1 mol/L KOH	1.60	nanosheets	on Ni foam	[20]
Ni-Co-P hollow nanobricks	1 mol/L KOH	1.62	nanobricks	on Ni foam	[21]

CoSe$_2$/MoSe$_2$ nanosheets	1 mol/L KOH	1.63	nanosheets	on carbon cloth	[22]
NiSe$_2$/CC-180	1 mol/L KOH	1.58	nanosheets	on carbon cloth	this work

[a] The voltage required to generate the current density is 10 mA cm^{-2} in overall water splitting.

References

[1] B. Delley, J. Chem. Phys. 92 (1990) 508-517.

[2] J.P. Perdew, K. Burke, M. Ernzerhof, Phys. Rev. Lett. 77 (1996) 3865-3868.

[3] S. Grimme, J. Comput. Chem. 25 (2004) 1463-1473.

[4] S. Grimme, J. Comput. Chem. 27 (2006) 1787-1799.

[5] C. Pi, Z. Zhao, X. Zhang, B. Gao, Y. Zheng, P.K. Chu, L. Yang, K. Huo, Chem. Eng. J. 416 (2021) 129130.

[6] J.K. Nørskov, T. Bligaard, A. Logadottir, J.R. Kitchin, J.G. Chen, S. Pandelov, U. Stimming, J. Electrochem. Soc. 152 (2005) J23.

[7] R. Gao, H. Zhang, D. Yan, Nano Energy 31 (2017) 90-95.

[8] X. Zheng, X. Han, H. Liu, J. Chen, D. Fu, J. Wang, C. Zhong, Y. Deng, W. Hu, ACS Appl. Mater. Interfaces 10 (2018) 13675-13684.

[9] K. Ao, J. Dong, C. Fan, D. Wang, Y. Cai, D. Li, F. Huang, Q. Wei, ACS Sustain. Chem. Eng. 6 (2018) 10952-10959.

[10] Y. Zhong, B. Chang, Y. Shao, C. Xu, Y. Wu, X. Hao, ChemSusChem 12 (2019) 2008-2014.

[11] A. Sivanantham, S. Shanmugam, Appl. Catal. B-Environ. 203 (2017) 485-493.

[12] J. Nai, H. Yin, T. You, L. Zheng, J. Zhang, P. Wang, Z. Jin, Y. Tian, J. Liu, Z. Tang, L. Guo, Adv. Energy Mater. 5 (2015) 1401880.

[13] L. Wang, X. Huang, J. Xue, ChemSusChem 9 (2016) 1835-1842.

[14] X. Han, X. Ling, D. Yu, D. Xie, L. Li, S. Peng, C. Zhong, N. Zhao, Y. Deng, W. Hu, Adv. Mater. 31 (2019) 1905622.

[15] X. Zhu, D. Zhang, C.-J. Chen, Q. Zhang, R.-S. Liu, Z. Xia, L. Dai, R. Amal, X. Lu, Nano Energy 71 (2020) 104597.

[16] C. Panda, P.W. Menezes, C. Walter, S. Yao, M.E. Miehlich, V. Gutkin, K. Meyer, M. Driess, Angew. Chem. Int. Ed. 56 (2017) 10506-10510.

[17] H. Wu, X. Lu, G. Zheng, G.W. Ho, Adv. Energy Mater. 8 (2018) 1702704.

[18] C. Tang, N. Cheng, Z. Pu, W. Xing, X. Sun, Angew. Chem. Int. Ed. 54 (2015) 9351-9355.

[19] J. Masud, A.T. Swesi, W.P. Liyanage, M. Nath, ACS Appl. Mater. Interfaces 8 (2016) 17292-17302.

[20] C. Hu, L. Zhang, Z.-J. Zhao, A. Li, X. Chang, J. Gong, Adv. Mater. 30 (2018) 1705538.

[21] Y. Chen, S. Ji, C. Chen, Q. Peng, D. Wang, Y. Li, Joule 2 (2018) 1242-1264.

[22] L. Xia, H. Song, X. Li, X. Zhang, B. Gao, Y. Zheng, K. Huo, P.K. Chu, Front. Chem. 8 (2020) 382.